Theory of corticothalamic brain activity in a spherical geometry: Spectra, coherence, and correlation

K. N. Mukta,* J. N. MacLaurin, and P. A. Robinson
School of Physics, University of Sydney, New South Wales 2006, Australia
and Center for Integrative Brain Function, University of Sydney, New South Wales 2006, Australia
(Received 2 July 2017; published 21 November 2017)

Corticothalamic neural field theory is applied to a spherical geometry to better model neural activity in the human brain and is also compared with planar approximations. The frequency power spectrum, correlation, and coherence functions are computed analytically and numerically. The effects of cortical boundary conditions and resulting modal aspects of spherical corticothalamic dynamics are explored, showing that the results of spherical and finite planar geometries converge to those for the infinite planar geometry in the limit of large brain size. Estimates are made of the point at which modal series can be truncated and it is found that for physiologically plausible parameters only the lowest few spatial eigenmodes are needed for an accurate representation of macroscopic brain activity. A difference between the geometries is that there is a low-frequency $1/f$ spectrum in the infinite planar geometry, whereas in the spherical geometry it is $1/f^2$. Another difference is that the alpha peak in the spherical geometry is sharper and stronger than in the planar geometry. Cortical modal effects can lead to a double alpha peak structure in the power spectrum, although the main determinant of the alpha peak is corticothalamic feedback. In the spherical geometry, the cross spectrum between two points is found to only depend on their relative distance apart. At small spatial separations the low-frequency cross spectrum is stronger than for an infinite planar geometry and the alpha peak is sharper and stronger due to the partitioning of the energy into discrete modes. In the spherical geometry, the coherence function between points decays monotonically as their separation increases at a fixed frequency, but persists further at resonant frequencies. The correlation between two points is found to be positive, regardless of the time lag and spatial separation, but decays monotonically as the separation increases at fixed time lag. At fixed distance the correlation has peaks at multiples of the period of the dominant frequency of system activity.

DOI: 10.1103/PhysRevE.96.052410

I. INTRODUCTION

Neural field theory (NFT) has been successfully used to analyze numerous brain activity phenomena [1–14]. In particular, a neural field corticothalamic model has been used to investigate the spectrum of activity fluctuations [15,16], age-related changes to the physiology of the brain [17], and evoked response potentials (ERPs) [18]. In most of these papers, the approximation of a planar geometry was used to reproduce and unify many features of brain activity and the resulting electroencephalogram [6,9,10,19–23], including the spectral peaks seen in waking and sleeping states [6,9,10,16], ERPs [18,24], measures of coherence, and spatiotemporal structure [25–27]. Measures such as electroencephalograms (EEGs) spectra, correlations, and coherence functions are widely used diagnostics of structure in these signals [6,21,28,29] and are often employed to probe cognitive events and information processing experimentally [28–30]. Notably, the parameters used in our neural field modeling have been found to be consistent with independent physiological estimates [31].

Our previous work [6] examined modal effects on white-noise-driven spectra in a planar system. This showed that the infinite case is an excellent approximation at most frequencies for systems of cortical circumference exceeding roughly 0.2 m, which is well fulfilled for humans, with exceptions at very low frequencies and near the alpha resonance. This work also found that the modal spectrum was dominated by the contributions from the spatially uniform global mode.

Some prior work has employed spherical models to analyze brain activity [28,32–41]. This is a better approximation to real brain geometry than a planar geometry. Nunez *et al.* [28,35,38–41] analyzed electroencephalographic (EEG) signals, correlation, and coherence functions on a spherical skull but did not consider individual brain hemispheres or the thalamus, which has been shown to be critical for a more realistic and general brain model [11,14,19,42].

In this work we use a spherical geometry to analyze activity via a corticothalamic model of one brain hemisphere, using spherical harmonic analysis. Indeed, our recent work [43] showed that the eigenmodes of a single brain hemisphere are close analogs of spherical harmonics. Spherical harmonics are well understood and have been applied to the approximation of brain surfaces [33] and many other applications such as spatial filtering, calculation of EEG coherence on the scalp [34], and brain imaging [36,44–49]. We also compare and contrast our work with our previous work in planar geometries [6,10,43]. Key issues that we address are what the effects of spherical geometry are on activity measures such as spectra, correlations, and coherences.

The structure of this paper is as follows. After briefly reviewing the neural field model of the corticothalamic system in Sec. II, we write down its transfer function in a form suited to application to a variety of geometries. In Sec. III we derive the power spectra for spherical and planar geometries and compare and discuss the results. In Sec. IV we derive the cross spectrum

*Corresponding author: School of Physics, University of Sydney, NSW 2006, Australia; kamrun.mukta@sydney.edu.au

for spherical and planar geometries and discuss the results. In Sec. V we derive coherence and correlation functions for these cases and analyze the results. Finally, Sec. VI presents a summary.

II. NEURAL FIELD THEORY OF THE CORTICOTHALAMIC SYSTEM

In this section we start with a brief review of the neural field corticothalamic model that we employ and then use it to determine the transfer function for neural activity in spherical and planar geometries [10,11,17,19,31,50,51]. This function is used to calculate the power spectrum, cross spectrum, coherence, and correlation functions in subsequent sections.

A. Corticothalamic model

The model used here has been widely employed in previous work [10,11,19] and incorporates the

populations and connections shown in Fig. 1: excitatory (e) and inhibitory (i) cortical neurons, thalamic relay neurons (s), thalamic reticular neurons (r), and external inputs (n) [10,12,18,19].

Mean firing rates Q_a of neurons are nonlinearly related to their mean soma potentials V_a by $Q_a(\mathbf{r},t) = S[V_a(\mathbf{r},t)]$, where S is a sigmoid function that increases from 0 to $Q_{\max}$ as V_a increases from $-\infty$ to ∞, with V_a measured relative to resting. We use

$$Q_a(\mathbf{r},t) = S[V_a(\mathbf{r},t)], \tag{1}$$

$$S[V_a(\mathbf{r},t)] = \frac{Q_{\max}}{1+\exp[-\{V_a(\mathbf{r},t)-\theta\}/\sigma']}, \tag{2}$$

where t is the time, θ is the mean neural firing threshold, $\sigma'\pi/\sqrt{3}$ is the standard deviation of the threshold, and $Q_{\max}$ is the maximum firing rate.

The potential V_a results from inputs ϕ_b from other populations b, with

$$D_\alpha V_a(\mathbf{r},t) = \sum_b \nu_{ab}\phi_b(\mathbf{r},t-\tau_{ab}), \tag{3}$$

$$D_\alpha = \frac{1}{\alpha\beta}\frac{d^2}{dt^2} + \left(\frac{1}{\alpha}+\frac{1}{\beta}\right)\frac{d}{dt} + 1, \tag{4}$$

with [9–11,16,20] $\nu_{ab} = s_{ab}N_{ab}$, where N_{ab} is the mean number of synapses to neurons of type a from type b and s_{ab} is the time-integrated strength of the response in neurons of type a to a unit signal from neurons of type b, implicitly weighted by the neurotransmitter release probability [12,20,31,50,52]. The time delays τ_{ab} arise from discrete anatomical separations between populations, and the characteristic rise time and decay time of the response at the cell body are parametrized by $1/\beta$ and $1/\alpha$, which can be different for each of the connections in the model [20] but are set equal here because they do not affect the modal structure, which is our main focus. The number of synapses within and between cortical populations is assumed to be proportional to the numbers of source and target neurons, consistent with physiology [53,54], which implies $\nu_{ee} = \nu_{ie}$, $\nu_{ei} = \nu_{ii}$, and $\nu_{es} = \nu_{is}$ [20,31,53]. Hence there are eight independent connection strengths in Fig. 1.

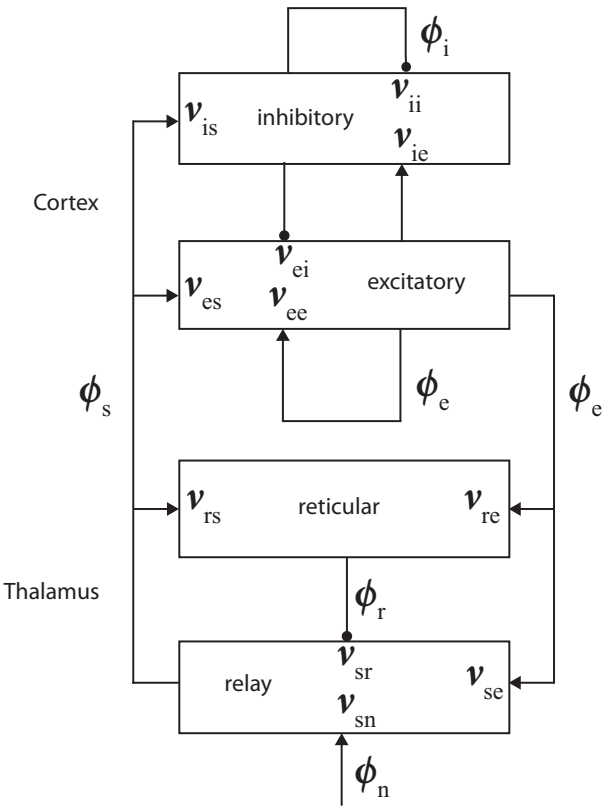

FIG. 1. Schematic diagram of corticothalamic neural field model of the system. The neural populations shown are cortical excitatory e, cortical inhibitory i, thalamic reticular r, and thalamic relay s. Each parameter ν_{ab} in Eq. (3) quantifies the connection to population a from population b. Excitatory connections are shown with pointed arrowheads and inhibitory connections are shown with round arrowheads.

The field $\phi_a(\mathbf{r},t)$ of outgoing activity propagates at an average speed v_a and approximately obeys a damped wave equation with a source Q_a [6,9–11,16,20,53], with

$$D_a(\mathbf{r},t)\phi_a(\mathbf{r},t) = Q_a(\mathbf{r},t), \tag{5}$$

$$D_a(\mathbf{r},t) = \frac{1}{\gamma_a^2}\frac{\partial^2}{\partial t^2} + \frac{2}{\gamma_a}\frac{\partial}{\partial t} + 1 - r_a^2\nabla^2, \tag{6}$$

where r_a is the mean range of axons a and $\gamma_a = v_a/r_a$ is the temporal damping rate [11,16]. To obtain spatially uniform steady states of the model, we set all of the time and space derivatives in (2)–(6) to zero. The steady-state value $\phi_e^{(0)}$ of ϕ_e then satisfies

$$\begin{aligned}\phi_e^{(0)} - (\nu_{ee}+\nu_{ei})\phi_e^{(0)} &= \nu_{es}S\Big[\nu_{es}\phi_e^{(0)} + \nu_{sr}S\Big(\nu_{re}\phi_e^{(0)} + (\nu_{rs}/\nu_{es})\\ &\quad\times\left\{S^{-1}\left[\phi_e^{(0)} - (\nu_{ee}+\nu_{ei})\phi_e^{(0)}\right]\right\}\Big)\nu_{sn}\phi_n^{(0)}\Big],\end{aligned} \tag{7}$$

where $\phi_n^{(0)}$ is the mean stimulus [20,31]. Steady-state values of the other $\phi_a^{(0)}$ can then be found from the above equations.

It has been extensively demonstrated that most normal brain activity can be approximated as being due to linear perturbations about a fixed point [6,10,11,15,16,31,50,52,55]. Hence, in the present work, we consider only the first term in

the Taylor expansion of Eq. (2), which yields

$$Q_a(\mathbf{r},t) - Q_a^{(0)} = \rho_a\big[V_a(\mathbf{r},t) - V_a^{(0)}\big], \tag{8}$$

where ρ_a is the derivative of the sigmoid function with respect to its argument at the fixed point, where $V_a = V_a^{(0)}$. By taking the Fourier transform of Eqs. (3)–(6) and (8), we can then express the firing rate ϕ_e in terms of the external signal ϕ_n. In particular, we find the transfer function $T(\mathbf{k},\omega)$, which is the cortical excitatory response per unit external stimulus and encapsulates the relative phase via its complex value [10,20]; it is the key to linear properties of the system and has the form

$$T(\mathbf{k},\omega) = \frac{\phi_e(\mathbf{k},\omega)}{\phi_n(\mathbf{k},\omega)}, \tag{9}$$

$$= \frac{A(\omega)}{k^2r_e^2 + q^2r_e^2}, \tag{10}$$

$$A(\omega) = \frac{L^2G_{esn}e^{i\omega t_0/2}}{(1-L^2G_{srs})(1-G_{ei}L)}, \tag{11}$$

$$q^2r_e^2 = \left(1-\frac{i\omega}{\gamma_e}\right)^2 - \frac{1}{1-G_{ei}L} \times \left\{LG_{ee} + \frac{\big[L^2G_{ese}+L^3G_{erse}\big]e^{i\omega t_0}}{1-L^2G_{srs}}\right\}, \tag{12}$$

$$L(\omega) = \left(1-\frac{i\omega}{\alpha}\right)^{-1}\left(1-\frac{i\omega}{\beta}\right)^{-1}, \tag{13}$$

where $\mathbf{k}$ is the wave vector, $k = 2\pi/\lambda$, λ is the wavelength, and $\omega = 2\pi f$ is the angular frequency, where f is the frequency in Hz. The gain $G_{ab} = \rho_a\nu_{ab} = \rho_b N_{ab}S_{ab}$ is the differential response in neurons a per unit input from neurons b. The quantities $G_{ese} = G_{es}G_{se}$, $G_{esre} = G_{es}G_{sr}G_{re}$, and $G_{srs} = G_{sr}G_{rs}$ correspond to the overall gains for the excitatory corticothalamic, inhibitory corticothalamic, and intrathalamic loops, respectively.

B. Solution of the Helmholtz equation

In the absence of external inputs Eq. (5) gives

$$D_a(\mathbf{r},t)\phi_a(\mathbf{r},t) = 0. \tag{14}$$

Analytically the solution of this equation can be approached via the ansatz

$$\phi_a(\mathbf{r},t) = R(\mathbf{r})\Theta(t), \tag{15}$$

where R and Θ depend only on r and t, respectively. After substituting Eq. (15) into Eq. (14) and then dividing by $R(\mathbf{r})\Theta(t)$, we obtain

$$\frac{1}{\gamma_e^2\Theta}\frac{d^2\Theta}{dt^2} + \frac{2}{\gamma_e\Theta}\frac{d\Theta}{dt} + 1 = r_e^2\frac{\nabla^2R}{R}. \tag{16}$$

We can separate the variables in Eq. (16) by introducing the ansatz

$$\phi_{ab} = y_\eta(\mathbf{r})e^{-i\omega_\eta t} \tag{17}$$

for a spatial eigenmode $y_\eta(\mathbf{r})$ with eigenfrequency ω_η, where η labels the eigenmode. Substituting this into Eq. (16) gives

$$r_e^2\frac{\nabla^2y_\eta(\mathbf{r})}{y_\eta(\mathbf{r})} = D_a(\omega). \tag{18}$$

This equation holds for all $\mathbf{r}$ and t. We observe that the left-hand side does not depend on t and right-hand side does not depend on $\mathbf{r}$. So the only possible solution is if they are both equal to a constant. We can set both sides of Eq. (18) equal to a separation constant $-k_\eta^2$, which yields

$$\nabla^2y_\eta(\mathbf{r}) = -k_\eta^2y_\eta(\mathbf{r}), \tag{19}$$

$$D_a(\omega_\eta) = -k_\eta^2r_e^2. \tag{20}$$

Equations (19) and (20) can be solved for the eigenmodes and corresponding eigenvalues of Eq. (19) for specific geometries, and corresponding eigenfrequencies can be obtained from Eq. (20) if required. Once we have the eigenvalue k_η^2 we can write the general transfer function as

$$T(k_\eta^2,\omega) = \frac{A(\omega)}{k_\eta^2r_e^2 + q^2r_e^2}, \tag{21}$$

where $A(\omega)$ is defined in Eq. (11).

For an infinite planar brain geometry the eigenmodes labeled $\mathbf{k}$ are Fourier modes, i.e.,

$$y_\eta(\mathbf{r}) = \exp(i\mathbf{k}\cdot\mathbf{r}), \tag{22}$$

$$k_\eta^2r_e^2 = k^2r_e^2. \tag{23}$$

where $\mathbf{k}$ is the wave vector. For any continuous function f on a two-dimensional (2D) plane, the Fourier transform is

$$f(\mathbf{r},\omega) = \int\frac{d^2\mathbf{k}}{(2\pi)^2}f(\mathbf{k},\omega)\exp(i\mathbf{k}\cdot\mathbf{r}), \tag{24}$$

where

$$f(\mathbf{k},\omega) = \int d^2\mathbf{r}\, f(\mathbf{r},\omega)\exp(-i\mathbf{k}\cdot\mathbf{r}). \tag{25}$$

In a finite planar geometry, we approximate the cortex as a rectangular sheet of size $L_x \times L_y$ and the modes have the form of the first of Eq. (22) but with $\mathbf{k} = \mathbf{k}_{mn} = (k_x, k_y)$ satisfying

$$k_x = \frac{2\pi m}{L_x}, \tag{26}$$

$$k_y = \frac{2\pi n}{L_y}, \tag{27}$$

where m and n are arbitrary integers. The Fourier transform on a 2D finite plane is the same as the infinite 2D plane, except that the integrals over $\mathbf{k}$ are replaced by sums over the allowed values, with

$$\int\frac{d^2\mathbf{k}}{(2\pi)^2} \to \frac{1}{L_xL_y}\sum_{m=-\infty}^{\infty}\sum_{n=-\infty}^{\infty}. \tag{28}$$

Thus we can write

$$f(\mathbf{r},\omega) = \frac{1}{L_xL_y}\sum_{m=-\infty}^{\infty}\sum_{n=-\infty}^{\infty}f(\mathbf{k}_{mn},\omega)\exp(i\mathbf{k}_{mn}\cdot\mathbf{r}), \tag{29}$$

$$f(\mathbf{k}_{mn},\omega) = \int d^2\mathbf{r}\, f(\mathbf{r},\omega)\exp(-i\mathbf{k}_{mn}\cdot\mathbf{r}). \tag{30}$$

In the case of a spherical geometry, considering a sphere of radius R_s, the eigenmodes are

$$y_{\ell m}(\theta,\phi) = Y_{\ell m}(\theta,\varphi), \tag{31}$$

where η has been replaced by ℓ and m, and the eigenmodes are the real spherical harmonics $Y_{\ell m}$. This is an approximation that has been extensively used to represent EEG activity on the scalp [28,39,43,56,57], albeit most often treating the whole brain, skull, and scalp as nested spheres; an exception was [43], which analyzed the activity eigenmodes of a single hemisphere of the brain. Now

$$k_{\ell m}^2 r_e^2 = \frac{r_e^2}{R_s^2}\ell(\ell+1). \tag{32}$$

Equation (32) shows that the eigenvalues depend only on the angular momentum mode number $\ell = 0,1,\ldots$ and are independent of the azimuthal mode number $m = -\ell,\ldots,\ell$.

Any continuous bounded function f on a sphere can be expanded in terms of real-valued spherical harmonics, with

$$f(\theta,\varphi) = \sum_{\ell m} f_{\ell m} Y_{\ell m}(\theta,\varphi), \tag{33}$$

$$f_{\ell m} = \iint f(\theta,\varphi) Y_{\ell m}(\theta,\varphi)\sin\theta\, d\theta\, d\varphi, \tag{34}$$

with ℓ being a non-negative integer and $-\ell \leqslant m \leqslant \ell$. In Eq. (33) the sum extends over all such ℓ and m, while the integral in Eq. (34) extends over the whole sphere. Here

$$Y_{\ell m}(\theta,\phi) = \begin{cases} c_{\ell m} P_\ell^{|m|}(\cos\theta)\sin(|m|\varphi), & -\ell \leqslant m \leqslant -1 \\ 2^{-1/2} c_{\ell m} P_\ell^0(\cos\theta), & m = 0 \\ c_{\ell m} P_\ell^{|m|}(\cos\theta)\cos(|m|\varphi), & 1 \leqslant m \leqslant \ell, \end{cases} \tag{35}$$

where

$$c_{\ell m} = \left[\frac{2\ell+1}{2\pi}\frac{(\ell-|m|)!}{(\ell+|m|)!}\right]^{1/2}$$

and the P_ℓ^m are the associated Legendre polynomials of order m [58].

III. POWER SPECTRUM

In this section we derive the form of the EEG spectrum from the transfer function Eq. (10) for infinite planar, finite planar, and spherical geometries. We then discuss the predictions of the model and compare the three geometries with each other.

A. Infinite planar brain geometry

The EEG power spectrum $P(\omega)$ is the average over all realizations, i.e., $\langle\phi_e(0,\omega)\phi_e(0,\omega)\rangle$. It can be calculated for the infinite planar case by integration of $|\phi_e(\mathbf{k},\omega)|^2$ over $\mathbf{k}$. In turn, we see from Eq. (10) that ϕ_e is equal to the multiplication of the transfer function by the white-noise stimulus. This means that, for continuum modes on the plane,

$$P(\omega) = \frac{1}{4\pi^2}\int \left|T(k_\eta^2,\omega)\right|^2 |\phi_n(\mathbf{k},\omega)|^2 d^2\mathbf{k}. \tag{36}$$

In the present work the input stimulus $\phi_n(\mathbf{k},\omega)$ is taken to be white noise [6,11,20,26,31,50,52] with uniform spectral power density, so $|\phi_n(\mathbf{k},\omega)|^2 = \phi_n^2$ is constant for nonzero $\mathbf{k}$ and ω. In the linear approximation, the value of $\phi_n(\mathbf{k},\omega)$ only affects the normalization of the power spectrum. Equation (36) yields

$$P(\omega) = \frac{\phi_n^2}{4\pi^2}\int |T(\mathbf{k},\omega)|^2 d^2\mathbf{k}, \tag{37}$$

$$= \frac{\left|A(\omega)\right|^2}{4\pi^2}\phi_n^2 \int \frac{d^2\mathbf{k}}{\left|k^2 r_e^2 + q^2 r_e^2\right|^2}, \tag{38}$$

where $A(\omega)$ and $q^2(\omega)$ are from Eqs. (11) and (12). Finally, we get [6,19,31]

$$P(\omega) = \frac{|A(\omega)|^2}{4\pi r_e^2}\left|\frac{\mathrm{Arg} q^2 r_e^2}{\mathrm{Im} q^2 r_e^2}\right|\phi_n^2. \tag{39}$$

TABLE I. Nominal corticothalamic model parameter values from previous work [16,19].

Symbol	Quantity	Value	Unit
α	synaptodendritic decay rate	83	s^{-1}
β	synaptodendritic rise rate	769	s^{-1}
t_0	corticothalamic loop delay	0.085	s
γ_e	cortical damping rate	116	s^{-1}
r_e	excitatory axon range	0.086	m
G_{ee}	excitatory cortical gain	2.07	
G_{ei}	inhibitory cortical gain	−4.11	
G_{ese}	excitatory cortical gain	5.98	
G_{esre}	excitatory inhibitory gain	−1.67	
G_{srs}	intrathalamic gain	−0.66	
k_0	low-pass cutoff	10	m^{-1}
L_x	cortical sheet length	0.5	m
L_y	cortical sheet width	0.5	m
R_s	radius of sphere	0.1	m

Table I summarizes typical values of the parameters of our model, as inferred from physiology and fits to EEG spectra [10]. We assume that only the corticocortical and corticothalamic connectivities shown in Fig. 1 are relevant and make the approximation that corticocortical connectivities are proportional to the numbers of synapses involved, which implies $V_i = V_e$ and $Q_i = Q_e$ [9,13] and lets us concentrate on excitatory quantities. The smallness of r_i, r_r, and r_s also lets us ignore all derivative terms in Eq. (6) [10,11], except for $a = e$. These approximations, and parameter values similar to those in Table I, have previously been shown to be in excellent agreement with spectra, impulse responses, and nonlinear dynamics of EEGs [6,9,18].

Figure 2 shows an illustrative spectrum obtained from Eq. (39) for the parameters in Table I and the infinite planar geometry. As in prior work [6], alpha and beta peaks, which are due to corticothalamic loop resonances, occur near 9.3 and 18.7 Hz, respectively [59]. The low-frequency spectrum with $P(f) \sim f^{-1}$ at 0.2–5 Hz reflects proximity to criticality, with a plateau below 0.2 Hz and at high frequencies we observe a fast falloff of the spectrum at $f \gtrsim 20$ Hz, caused by the onset of synaptodendritic low-pass filtering [9–11,59,60]. Note that $P(f) = 2\pi P(\omega)$ because $\omega = 2\pi f$.

The term q^2 is very important because it is a key indicator of the resonance of the system at a particular frequency.

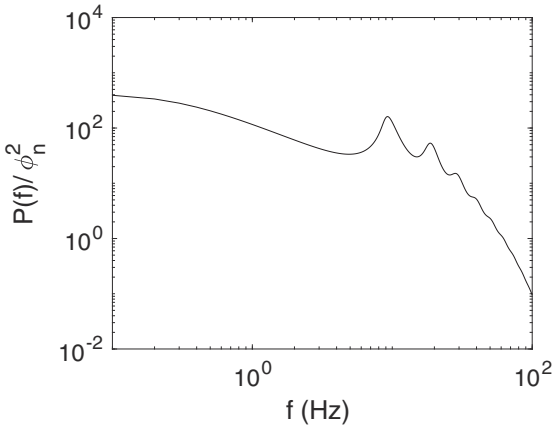

FIG. 2. Frequency spectrum for waking stage (eyes closed) for the parameters listed in Table I and an infinite planar geometry.

From Eq. (39) we see that if $|\mathrm{Im}q^2r_e^2| \ll |\mathrm{Arg}(q^2r_e^2)|$, then the power spectrum must be large, which corresponds to a strong resonance. Figure 3 shows the corresponding locus of $q^2(\omega)r_e^2$ for $\omega > 0$ obtained from Eq. (39) for parameters in Table I. As in prior work [9–11], after starting near the origin at $f = 0$, q^2 increases in modulus, with $|q^2(\omega)| \propto \omega$ approximately for 0.3 Hz $\lesssim f \lesssim 4$ Hz, where $P(f) \propto f^{-1}$. The locus of q^2 exhibits loops as ω increases away from zero, which cause $\mathrm{Im}q^2r_e^2$ to oscillate due to corticothalamic feedback. Thus the first, second, third, and fourth peaks that can be observed in Fig. 3 correspond, respectively, to the $f = 0$, alpha, beta, and gamma peaks in the power spectrum.

B. Two-dimensional finite brain geometry

In a finite system, the integral in Eq. (36) becomes a summation over spatial modes

$$P(\omega) = \sum_{\eta} \left|T\left(k_\eta^2,\omega\right)\right|^2 |\phi_n(\mathbf{k},\omega)|^2. \tag{40}$$

For a 2D rectangular cortex of dimensions $L_x \times L_y$ with periodic boundary conditions, the power spectrum $P(\omega)$

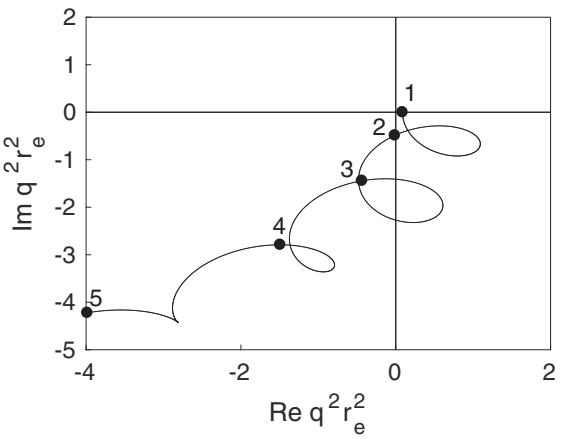

FIG. 3. Locus of $q^2(\omega)r_e^2$ for $\omega > 0$ and parameters in Table I, where ω ranges from 0 (point 1) to 251 s^{-1} (point 5). The alpha, beta, and gamma peaks are indicated by points 2, 3, and 4, respectively.

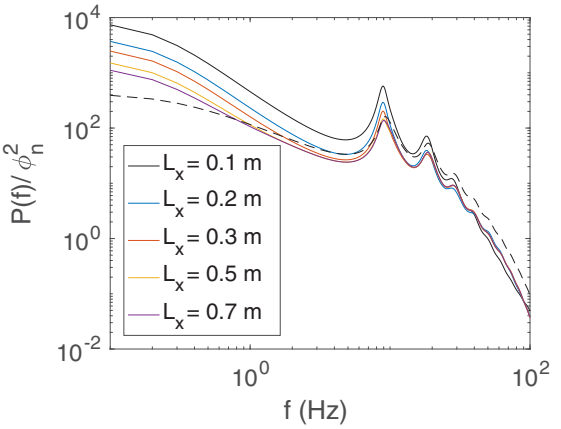

FIG. 4. Frequency spectra for the parameters listed in Table I for infinite and finite 2D cases with $L_x = L_y$. The case of infinite geometry is shown as a dashed line and the finite geometry as a solid line. Here a finite geometry is shown with increasing L_x values from 0.1 m (top) to 0.7 m (bottom), as indicated in the legend.

is [6]

$$P(\omega) = \frac{|A(\omega)|^2}{r_e^4}\frac{\phi_n^2}{L_xL_y}\sum_{m,n=-\infty}^{\infty}\frac{1}{\left|\left(\frac{2\pi m}{L_x}\right)^2+\left(\frac{2\pi n}{L_y}\right)^2+q^2\right|^2}, \tag{41}$$

$$= \frac{1}{r_e^4}\frac{|A(\omega)|^2\phi_n^2}{L_y}\sum_{n=-\infty}^{\infty}\frac{\mathrm{Im}\left[q_n\tilde{}\coth(q_n^*L_x/2)\right]}{2|q_n^2|\mathrm{Im}(q_n^2)}, \tag{42}$$

$$q_n^2 = q^2 + (2\pi n/L_y)^2. \tag{43}$$

Figure 4 shows spectra calculated for the parameters in Table I, using Eq. (42) for a 2D cortex with L_x varied and $L_x = L_y$ and the low-frequency spectrum has $P(f) \sim f^{-2}$.

At frequencies above ∼1 Hz with $L_x = L_y$ the spectrum rapidly approaches the infinite planar case as $L_x = L_y$ increases beyond ∼0.2 m, and at $f \gtrsim 30$ Hz, we observe a fast falloff of the spectra, as in the infinite case, which is also shown for comparison. At frequencies greater than or approximately equal to 9 Hz, as L_x decreases the alpha and beta peaks become sharper and the number of peaks increases. This is due to the increased influence of modal phenomena for small L_x. This effect is evident from Eq. (42), since the resonances occur when

$$q^2r_e^2 \approx -k_{mn}^2r_e^2 = -(2\pi r_e)^2\left(\frac{m^2}{L_x^2}+\frac{n^2}{L_y^2}\right) \tag{44}$$

for integers m and n. Clearly, these resonances occur on the negative half of the real axis. Since $q^2 \simeq 0$ only in the neighborhood of the origin, if L_x and L_y are small, then only low modes can satisfy the above relation. Furthermore, these resonances are spaced further apart for small L_x and L_y, so they are more easily distinguished; in the limit $L_x, L_y \to 0$ there is only one resonant mode. Conversely, if L_x and L_y are large, then while there may be many resonant modes, the resonances are close together and therefore modal effects cannot be distinguished in the spectra. The main difference between the 2D infinite and finite geometries is that at small

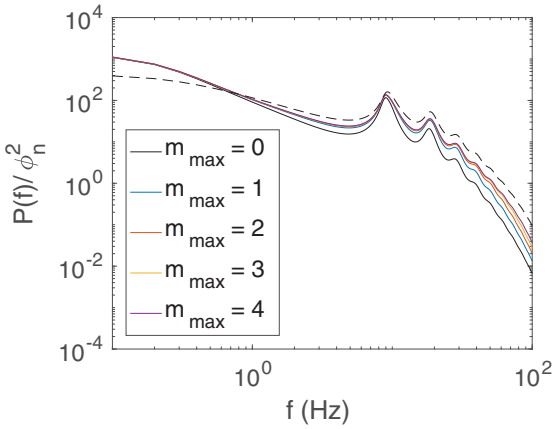

FIG. 5. Frequency spectra for the parameters listed in Table I for infinite (dashed line) and finite (solid line) planar geometry in a 2D cortex. Increasing $m_{\max}$ values are as shown from 0 (bottom) to 4 (top), as indicated in the legend.

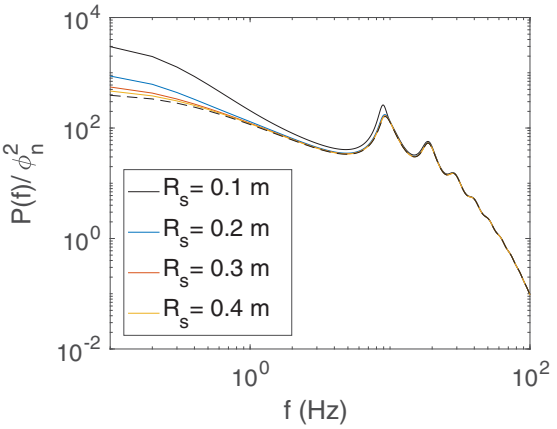

FIG. 6. Frequency spectra for the parameters listed in Table I for spherical geometry at various R_s, as indicated in the legend (solid lines), and for the infinite planar (dashed line) geometry.

L_x, there is a large enhancement in the low-frequency part of the spectrum, reflecting the strong role of the uniform ($\mathbf{k} = 0$) mode in this case because other modal resonances occur at large negative q^2 for small L_x.

To determine which modes contribute strongly with $L_x = L_y = 0.5$ m, in Fig. 5 we truncate the power spectrum summation from Eq. (42) to low-order modes with

$$(m^2 + n^2)^{1/2} \leqslant m_{\max}. \tag{45}$$

We observe that a good approximation is provided by $m_{\max} = 3$ up to 30 Hz, which is confirmed by the results in Fig. 5, which show rapid convergence as $m_{\max}$ increases beyond about 2. The number of modes that contribute significantly is greater than in one dimension because of the larger high-k weighting in 2D Fourier space. If they are weakly damped, resonant modes satisfy Eq. (44). Furthermore, it can be observed in Fig. 5 that the low-frequency enhancement has $P(f) \sim f^{-2}$ at $m_{\max} = 0$. It can be seen from Eq. (42) that resonance occurs when the locus of q^2 in Fig. 3 passes near the negative real axis, since in this regime $\mathrm{Im}(q^2) \simeq 0$, but not too far apart, which we have explained in Fig. 3.

C. Spherical brain geometry

The spectral decomposition of the activity relative to spherical coordinates is

$$\phi_e(\theta,\varphi,\omega) = \sum_{\ell=0}^{\infty}\sum_{m=-\ell}^{\ell} T_{\ell m}(\omega)\phi_n(\ell,m,\omega)Y_{\ell m}(\theta,\varphi). \tag{46}$$

For spherical geometry, the power spectrum is then

$$P(\omega) = \sum_{\ell=0}^{\infty}\sum_{m=-\ell}^{\ell} |T_{\ell m}(\omega)|^2 |\phi_n(\ell,m,\omega)|^2 |Y_{\ell m}(\theta,\varphi)|^2. \tag{47}$$

From the definition of the transfer function in Eq. (21),

$$T_{\ell m} = \frac{\phi_e(\ell,m,\omega)}{\phi_n(\ell,m,\omega)}, \tag{48}$$

$$= \frac{A(\omega)}{\ell(\ell+1)r_e^2/R_s^2 + q^2 r_e^2}, \tag{49}$$

which is independent of m. We can thus simplify the expansion for $P(\omega)$ for white noise, which has $|\phi_n(\ell,m,\omega)|^2 = \text{const}$, by using the addition formula for spherical harmonics [61]. This allows us to write

$$\sum_{m=-\ell}^{\ell} Y_{\ell m}(\theta,\varphi)^2 = \frac{2\ell+1}{4\pi}. \tag{50}$$

Equation (47) yields

$$P(\omega) = \frac{\phi_n^2 |A(\omega)|^2}{4\pi R_s^2} \sum_{\ell=0}^{\infty} \frac{2\ell+1}{\left|\ell(\ell+1)r_e^2/R_s^2 + q^2 r_e^2\right|^2} \tag{51}$$

$$= \frac{\phi_n^2 R_s^2}{4\pi r_e^4} |A(\omega)|^2 \sum_{\ell=0}^{\infty} \frac{2\ell+1}{\left[\ell(\ell+1) + \mathrm{Re}q^2 R_s^2\right]^2 + \left[\mathrm{Im}q^2 R_s^2\right]^2}. \tag{52}$$

Figure 6 shows illustrative spectra obtained from Eq. (52) for the parameters in Table I for spherical and infinite planar geometries with R_s varied. As $R_s \to \infty$, the spherical and infinite planar cases converge, as one would expect on physical grounds. This is because the sum in Eq. (52) approximates the integral that appears in Eq. (38) for the power spectrum in an infinite planar geometry, so that as $R_s \to \infty$, the power spectrum in the spherical geometry converges to the power spectrum in the infinite planar geometry, as expected on physical grounds. This is analogous to the convergence of the planar geometry to the infinite planar geometry as $L_x \to \infty$. We use $R_s \approx 0.1$ m for one cortical hemisphere, based on the requirement that the total area of the two hemispheres must match the observed 0.25 m^2 of the typical whole adult cortex [62]. This implies that the coefficient of $\ell(\ell+1)$ on the right-hand side of Eq. (32) is $(r_e/R_s)^2 \approx 0.74$ since $r_e \approx 0.086$ m [16,19,43]. For $R_s = 0.1$ m, the low-frequency enhancement has $P(f) \sim f^{-2}$ at 0.4–4 Hz, as shown in Fig. 6, because the uniform mode ($\ell = m = 0$) is dominant, just like in the finite planar geometry, which as we have seen also has a low-frequency enhancement of $P(f) \sim f^{-2}$. As in previous cases, we observe a plateau below 0.2 Hz and a

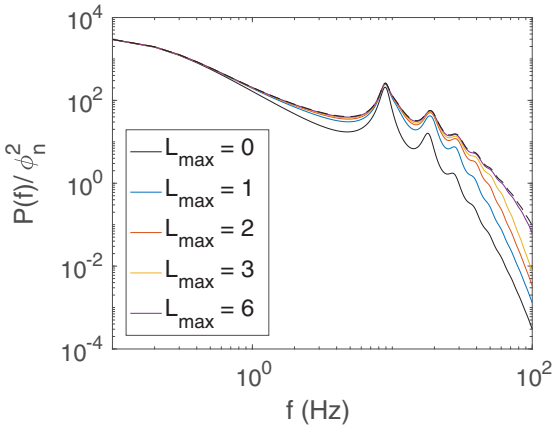

FIG. 7. Frequency spectra for the parameters listed in Table I for spherical geometry (solid lines), with $R_s = 0.1$ m, where the dashed line corresponds to the $L_{max} \approx \infty$ case and the solid lines are for increasing L_{max} values from 0 (bottom) to 6 (top), as indicated in the legend.

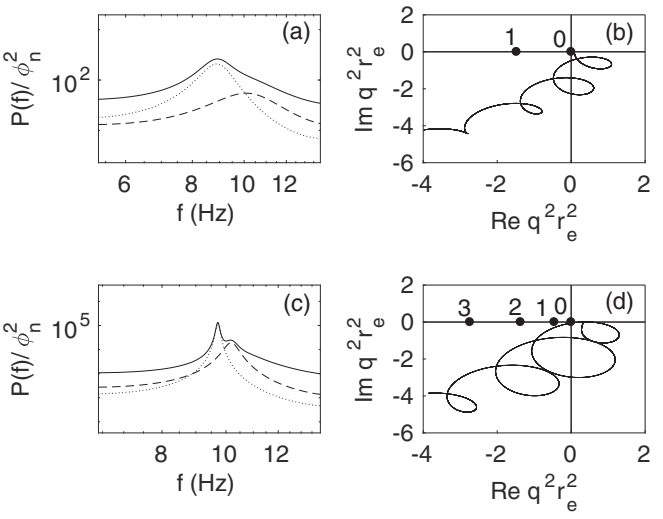

FIG. 8. Frequency spectra near the alpha peak and loci of $q^2 r_e^2$. (a) Spectrum for the parameters in Table I, where the solid line is the sum of all the modes, the dotted line is the $\ell = 0$ contribution, and the dashed line is the $\ell = 1$ contribution. (b) Locus of $q^2(\omega) r_e^2$ for the case in (a) and $\omega > 0$ (ω increases from zero at the point on the real axis toward the lower left). The locations of the poles for $\ell = 0,1$ are shown by the labeled dots. (c) Spectrum for the parameters in Table I except for $G_{es} = 4.5$, $G_{se} = 2.7$, and $R_s = 0.18$, where the solid line is the sum of all the modes, the dotted line is the $\ell = 0$ contribution, and the dashed line is the $\ell = 1$ contribution. (d) Locus of $q^2(\omega) r_e^2$ for the case in (c) and $\omega > 0$. The locations of the poles for $\ell = 0,1,2,3$ are shown by the labeled dots.

fast falloff of the spectra at $f \gtrsim 20$ Hz due to synaptodendritic low-pass filtering. The alpha and beta peaks are seen at ~8.9 and ~18.8 Hz, respectively. At $\omega \gtrsim \gamma_e$ we have $|qr_e| \simeq \omega/\gamma_e$, so modes that contribute significantly to $P(\omega)$ must satisfy $\ell(\ell+1) r_e^2/R_s^2 \lesssim |qr_e|^2 \simeq \omega^2/\gamma_e^2$ in Eq. (52). Hence, at $\omega \gtrsim \gamma_e$, the significant ℓ modes satisfy $\ell \lesssim L_{max} \lesssim \omega R_s/v_e$, giving a total of $\sim(\omega R_s/v_e)^2$ significant modes. We find in particular that only a modest number of modes with $\ell \lesssim 2$ should contribute strongly for $f \lesssim 30$ Hz for the parameters in Table I.

From Eq. (52) we see that $P(\omega)$ is large if $\ell(\ell+1) + \mathrm{Re} q^2 R_s^2 \simeq 0$ and $\mathrm{Im} q^2 R_s^2 \simeq 0$. When this happens, there are strong modal resonances and the system's behavior is very different from the infinite planar case. Indeed, this is why at low frequencies the power spectrum decreases as R_s increases, since there is a decrease of energy in the $\ell = 0$ mode. This is because the second denominator in Eq. (51) is of the form $\ell(\ell+1)/R_s^2$, which clearly goes to zero as $R_s \to \infty$.

The main difference between the spherical brain geometry and infinite planar geometry is that the alpha resonance is sharper and stronger in the spherical geometry due to the strong role of the uniform ($\ell = 0$) mode when energy is partitioned into discrete modes. To observe which modes contribute the most on the spherical geometry in Fig. 7, we truncate the power spectrum summation in Eq. (52) to low-order modes with $\ell \leqslant L_{max}$, with $L_{max} = 1$ sufficing at $f = 0$, and $L_{max} = 5$–6 at $f \simeq 10^2$ Hz. This can be seen in Fig. 7, with the first (spatially uniform) mode dominating until the alpha peak. The power spectrum asymptotes to zero for large ω, so that even though the relative strength of the higher-order modes increases, their absolute power is not great.

Weak substructure exists in the alpha peak in Fig. 7, which arises from the effect of purely cortical eigenmodes in frequency ranges where damping has been reduced by the corticothalamic resonance. We have shown previously that the major EEG peaks are due to resonances in a corticothalamic feedback loop [6,59]. To see this substructure more clearly, we expand Fig. 7 in the vicinity of the alpha peak, as shown in Fig. 8(a). It can be seen that the main peak near 9 Hz is due to $\ell = 0$ contributions, while the shoulder on the peak is due to $\ell = 1$ contributions that peak at around 10 Hz. Figure 8(b) shows the corresponding locus of $q^2(\omega) r_e^2$ for $\omega > 0$ and the parameters in Table I. The poles of (51) for $\ell = 0$ and 1 are indicated by the black dots on the $\mathrm{Re} q^2(\omega) r_e^2$ axis. It can be seen that the $\ell = 0$ pole is much closer to the locus of $q^2(\omega) r_e^2$ than the $\ell = 1$ pole, which is why the $\ell = 1$ contribution to the alpha peak is relatively weak. To illustrate substructure in the alpha peak more clearly, we modified three of the parameters in Table I to $G_{es} = 4.5$, $G_{se} = 2.7$, and $R_s = 0.18$ m to increase the radius of the loops in the $q^2 r_e^2$ plot and bring the $\ell = 1$ pole closer to the origin. The resulting power spectrum in Fig. 8(c) shows that the $\ell = 0$ and 1 contributions peak at 9.7 and 10.2 Hz, respectively, and that the latter is strong enough to produce a clear double peak in the power spectrum. Figure 8(d) shows the corresponding locus of $q^2(\omega) r_e^2$ for $\omega > 0$ for the modified parameters of Fig. 8(c). It can be seen that this locus approaches both the $\ell = 0$ and $\ell = 1$ poles closely. Hence we conclude that for brains with strong corticothalamic feedback and with large radii (such as in some very large mammals such as elephants and whales), there would be more likely to be a splitting of the alpha peak, but we have not explored whether other combinations of parameters might also yield splitting for smaller brain sizes.

IV. CROSS SPECTRUM

The cross power spectrum is a measure of the relationship at a particular frequency of two time series at different spatial points [34,63]. It is the expected value of the activity (i.e.,

the average over all possible realizations of the system) at a particular frequency and due to the generalized Wiener-Khintchine theorem it can be written as the inverse Fourier transform of the correlation function, with [16]

$$P(\mathbf{r},\mathbf{r}',\omega) = \int e^{i\omega T} C(\mathbf{r},\mathbf{r}',T)dT \tag{53}$$

$$= \langle \phi_e(\mathbf{r},\omega)\phi_e^*(\mathbf{r}',\omega)\rangle. \tag{54}$$

Here we consider only the infinite planar and spherical geometries because in the previous section we found that the modal effects in spherical geometry are similar to those in the finite planar case.

A. Infinite planar brain geometry

In the 2D continuum limit in which spatial boundary conditions on the cortex can be ignored, Eqs. (21) and (53) imply that

$$P(\mathbf{R},\omega) = \frac{|A(\omega)|^2\phi_n^2}{4\pi^2 r_e^4}\int \frac{e^{i\mathbf{k}\cdot\mathbf{R}}F(k)}{|k^2+q^2|^2}d^2\mathbf{k}, \tag{55}$$

where A(ω) is from Eq. (11) and in the case of EEG spectra, the filter function $F(k)$ approximates low-pass spatial filtering due to volume conduction in the skull and scalp. The assumption of random-phase white noise implies that the noise is delta correlated in wave number.

Filtering of high spatial frequencies k can be significant, as found by Srinivasan *et al.* [34]. The k dependence of their low-to-moderate wave number results is reasonably well fitted by a spatial filter of the form

$$F(k) = \frac{k_0^2}{k^2+k_0^2}, \tag{56}$$

where $F(k)$ is the square of the ratio of scalp to cortical voltage and $k_0 \approx 10\,\mathrm{m}^{-1}$ for scalp recordings [9,16,27]. For simplicity, we have ignored the factor $F(k)$ in our power spectrum section Eq. (39). Using this function we find

$$P(\mathbf{R},\omega) = \frac{|A(\omega)|^2\phi_n^2}{4\pi^2 r_e^4}\int \frac{e^{i\mathbf{k}\cdot\mathbf{R}}k_0^2}{|k^2+q^2|^2\left(k^2+k_0^2\right)}d^2\mathbf{k} \tag{57}$$

$$= \frac{|A(\omega)|^2\phi_n^2 k_0^2}{4\pi r_e^4}\int_0^\infty \frac{J_0(kR)d(k^2)}{|k^2+q^2|^2\left(k^2+k_0^2\right)} \tag{58}$$

$$= \frac{|A(\omega)|^2\phi_n^2}{2\pi r_e^4 \mathrm{Im}q^2}\mathrm{Im}\left[\frac{K_0(q^*R)-K_0(k_0R)}{1-q^{*2}/k_0^2}\right], \tag{59}$$

where J_0 is a Bessel function and K_0 is a Macdonald function (a modified Bessel function of the second kind) [16].

The limit $k_0 \to \infty$ in Eq. (59) implies that

$$P(R,\omega) = \frac{|A(\omega)|^2\phi_n^2}{2\pi r_e^4 \mathrm{Im}q^2}\mathrm{Im}[K_0(q^*R)]. \tag{60}$$

If we further take the limit $R \to 0$, the small argument limit of K_0 [16] in Eq. (60) implies that

$$P(0,\omega) = \frac{|A(\omega)|^2\phi_n^2}{4\pi r_e^2}\left|\frac{\mathrm{Arg}q^2r_e^2}{\mathrm{Im}q^2r_e^2}\right|, \tag{61}$$

which reproduces Eq. (39) for the power spectrum. If the limit $R \to 0$ is taken first in Eq. (59) and we write $q = |q|\exp(i\theta)$,

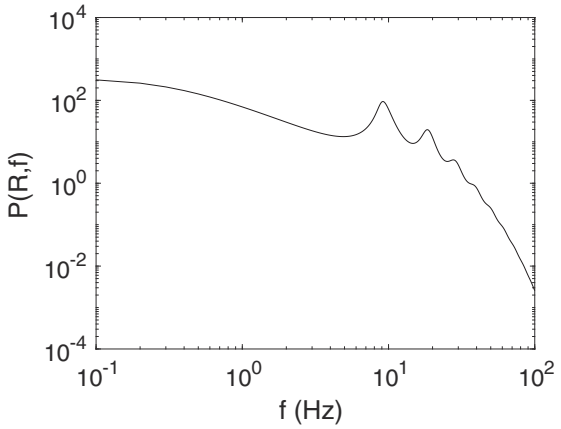

FIG. 9. Plot of the cross spectrum [Eq. (59)] for the infinite planar geometry and the parameters in Table I, for points at a distance $R = 0.017$ m apart, and $k_0 = 10\,\mathrm{m}^{-1}$.

we obtain

$$P(0,\omega) = \frac{|A(\omega)|^2\phi_n^2}{2\pi r_e^4 \mathrm{Im}q^2}\lim_{R\to 0}\mathrm{Im}\left[\frac{K_0(q^*R)-K_0(k_0R)}{1-q^{*2}/k_0^2}\right] \tag{62}$$

$$= \frac{|A(\omega)|^2\phi_n^2}{2\pi r_e^4 \mathrm{Im}q^2}\frac{1}{\left|1-q^{*2}/k_0^2\right|^2} \times \mathrm{Im}\left[\left(1-q^2/k_0^2\right)\{i\,\mathrm{Arg}q - \ln(|q|/k_0)\}\right] \tag{63}$$

$$= \frac{|A(\omega)|^2\phi_n^2}{4\pi r_e^2 \mathrm{Im}\left(q^2r_e^2\right)}\frac{1}{\left|1-q^{*2}/k_0^2\right|^2} \times \left\{\mathrm{Arg}\left(q^2r_e^2\right)\left[1-\mathrm{Re}\left(q^2/k_0^2\right)\right] + \mathrm{Im}\left(q^2/k_0^2\right)\ln(|q|/k_0)\right\}, \tag{64}$$

which generalizes Eq. (39) to $k_0 \neq \infty$.

Figure 9 shows an illustrative cross spectrum obtained from Eq. (59) for parameters in Table I with the value of $R = 0.017$ m and the infinite planar geometry. The alpha and beta peaks are seen near 9.1 and 18.4 Hz, respectively. These locations are very similar to the locations of the alpha and beta peaks for the power spectrum (i.e., when $R = 0$) that we discussed in Sec. III. This is due to the extra structure in the cross spectrum that results from the multiplicative factor involving Macdonald functions. The low-frequency cross spectrum $P(f) \sim f^{-1}$ at 0.5–5 Hz. We observe a plateau below 0.5 Hz. At high frequencies we observe a fast falloff of spectra at $f \gtrsim 19$ Hz. As for the power spectrum, only a modest number of modes contribute strongly to observed cross spectra for typical EEG frequencies of $f \lesssim 30$ Hz.

B. Spherical brain geometry

The cross spectrum between points with coordinates (θ,φ) and (θ',φ') and at frequency ω is

$$P(\theta,\varphi,\theta',\varphi',\omega) = \langle \phi_e(\theta,\varphi,\omega),\phi_e^*(\theta',\varphi',\omega)\rangle, \tag{65}$$

where the angular brackets indicate an average over all realizations. According to the white-noise assumption,

$$\langle \phi_n(\ell,m,\omega),\phi_n^*(\ell',m',\omega)\rangle = \delta_{\ell\ell'}\delta_{mm'}\phi_n^2. \tag{66}$$

We can therefore use Eq. (65) to obtain

$$P(\theta,\varphi,\theta',\varphi',\omega) = \frac{|A(\omega)|^2\phi_n^2}{R_s^2}\sum_{\ell=0}^{\infty}\sum_{m=-\ell}^{\ell}\frac{1}{\left|\ell(\ell+1)r_e^2/R_s^2+q^2r_e^2\right|^2} \times Y_{\ell m}(\theta,\varphi)Y_{\ell m}(\theta',\varphi'). \quad (67)$$

Using the addition theorem of spherical harmonics in Eq. (67), we then find

$$P(\theta,\varphi,\theta',\varphi',\omega) = \frac{|A(\omega)|^2\phi_n^2}{4\pi R_s^2}\sum_{\ell=0}^{\infty}\frac{2\ell+1}{\left|\ell(\ell+1)r_e^2/R_s^2+q^2r_e^2\right|^2}P_\ell(\cos\gamma), \quad (68)$$

where γ is the central angle between the points (θ,φ) and $(\theta',\varphi')'$, i.e., $\cos(\gamma)=\cos(\theta)\cos(\theta')+\sin(\theta)\sin(\theta')\cos(\varphi-\varphi')$. This means that the cross power spectrum is only a function of the central angle between the two points, which is what one would expect given that the system is invariant under a rotation of the sphere. We can therefore reorient our coordinate axes so that one point has spherical coordinates (0,0) and the other point has spherical coordinates $(\theta,0)$, i.e., the central angle between the points is θ.

To calculate scalp EEG spectra, rather than intracranial ones at the cortical surface, one must consider the possibility of filtering due to shielding that results from volume conduction by the cerebrospinal fluid, skull, and the scalp itself [9,28,34,35]. Incorporation of a filter function $F(\ell)$ in Eq. (68) yields

$$P(\theta,\omega) = \frac{|A(\omega)|^2}{4\pi R_s^2}\sum_{\ell=0}^{\infty}\frac{2\ell+1}{\left|\ell(\ell+1)r_e^2/R_s^2+q^2r_e^2\right|^2} \times P_\ell(\cos\theta)F(\ell). \quad (69)$$

A suitable approximate form when $\ell_0\sim k_0$ and $R_s\sim 1$ is

$$F(\ell) = \frac{\ell_0^2}{\ell^2+\ell_0^2}, \quad (70)$$

with $F(\ell)\to 1$ as $\ell_0\to\infty$. At $\theta=0$ we find

$$P(0,\omega) = \frac{|A(\omega)|^2}{4\pi R_s^2}\sum_{\ell=0}^{\infty}\frac{2\ell+1}{\left|\ell(\ell+1)r_e^2/R_s^2+q^2r_e^2\right|^2}, \quad (71)$$

where $A(\omega)$ is given in Eq. (11), which reproduces our previous power spectrum in Eq. (52).

Figure 10 explores the dependence of the spherical cross spectrum on the central angle θ. From Fig. 10 we observe that at low frequency, the cross spectrum is almost invariant with respect to θ. This illustrates the dominance of the spatially uniform spherical mode (i.e., $\ell=0$) at a spherical radius of $R_s=0.1$ m. For a larger value of R_s, this mode would be less dominant and the cross spectrum would vary more with θ. As frequency increases, the relative differences between the cross spectra at different values of θ increases. At small θ the low-frequency cross spectrum is stronger than for a infinite planar geometry and the alpha peak is sharper and stronger due to the partitioning of the energy into discrete modes.

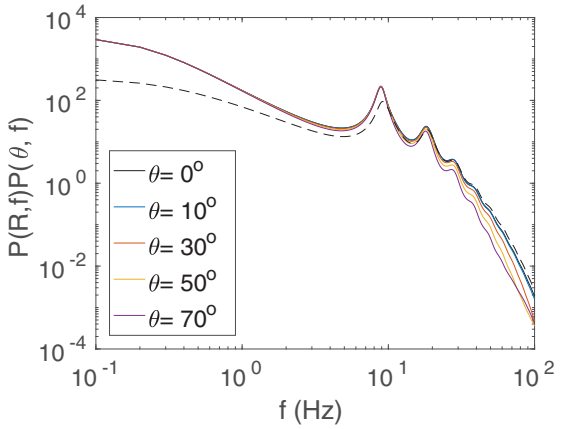

FIG. 10. Cross spectra in a spherical geometry with $R_s=0.1$ m for various θ for the parameters listed in Table I, as indicated in the legend. The dashed line is for the same parameters in an infinite planar geometry.

V. COHERENCE AND CORRELATION FUNCTIONS

The correlation function $C(\mathbf{r},\mathbf{r}',T)$ can be defined by

$$C(\mathbf{r},\mathbf{r}',T) = \langle\phi_e(\mathbf{r},t)\phi_e(\mathbf{r}',t-T)\rangle, \quad (72)$$

where angular brackets denote an average over t (a statistically steady state is assumed). The correlation function is a measure of the agreement between signals coming from different areas of the brain. Correlations in EEG signals lead to a deeper understanding of the functional organization of the brain [64]. Due to the Wiener-Khintchine theorem, the correlation function is equal to the inverse Fourier transform of the cross spectrum [16]. The normalized correlation function $\rho(\mathbf{r},\mathbf{r}',T)$ can be defined as

$$\rho(\mathbf{r},\mathbf{r}',T) = \frac{C(\mathbf{r},\mathbf{r}',T)}{[C(\mathbf{r},\mathbf{r},0)C(\mathbf{r}',\mathbf{r}',0)]^{1/2}}, \quad (73)$$

which satisfies $|\rho|\leqslant 1$. The coherence function is obtained by normalizing the correlation function, i.e.,

$$\gamma(\mathbf{r},\mathbf{r}',\omega) = \frac{P(\mathbf{r},\mathbf{r}',\omega)}{[P(\mathbf{r},\mathbf{r},\omega)P(\mathbf{r}',\mathbf{r}',\omega)]^{1/2}}, \quad (74)$$

which satisfies $|\gamma|\leqslant 1$.

A. Infinite planar brain geometry

From Eq. (74) the normalized coherence function for infinite planar geometry is given by [6]

$$\gamma(R,\omega) = \frac{2\,\mathrm{Im}K_0(q^*R)}{\mathrm{Arg}q^2r_e^2} \quad (75)$$

for $k_0=\infty$ and $R=|\mathbf{R}|=|\mathbf{r}-\mathbf{r}'|$. The correlation function is obtained by inverse Fourier transformation of the cross spectrum in Eq. (59),

$$C(R,T) = \frac{1}{4\pi^2r_e^2}\int e^{-i\omega T}\frac{|A(\omega)|^2}{\mathrm{Im}q^2r_e^2} \times \mathrm{Im}\left[\frac{K_0(q^*R)-K_0(k_0R)}{1-q^{*2}/k_0^2}\right]d\omega. \quad (76)$$

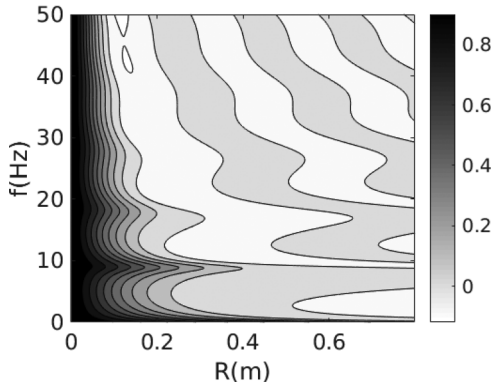

FIG. 11. Plot of the normalized coherence function $\gamma(R,\omega)$ vs R and $f = \omega/2\pi$, of a 2D infinite planar geometry for the parameters in Table I.

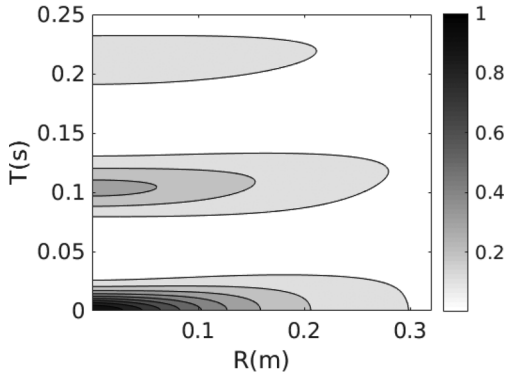

FIG. 12. Plot of the normalized correlation $\rho(R,T)$ vs R and T of the infinite planar geometry, for the parameters in Table I with $R_s = 0.1$ m.

The normalized correlation function is

$$\rho(R,T) = \frac{g(R,T)}{g(0,0)}, \tag{77}$$

where

$$g(R,T) = \frac{1}{4\pi^2 r_e^2}\int e^{-i\omega T}\frac{|A(\omega)|^2}{\mathrm{Im}q^2 r_e^2} \times \mathrm{Im}\left[\frac{K_0(q^*R) - K_0(k_0R)}{1 - q^{*2}/k_0^2}\right]d\omega. \tag{78}$$

In the limit $k_0 \to \infty$ we find

$$g(R,T) = \frac{1}{4\pi^2 r_e^2}\int e^{-i\omega T}\frac{|A(\omega)|^2}{\mathrm{Im}q^2 r_e^2}\mathrm{Im}[K_0(q^*R)]d\omega, \tag{79}$$

$$g(0,0) = \frac{1}{2\pi r_e^2}\int |A(\omega)|^2\frac{\mathrm{Arg}q^2 r_e^2}{\mathrm{Im}q^2 r_e^2}d\omega. \tag{80}$$

Figure 11 shows the 2D infinite planar geometry coherence functions obtained from Eq. (75) for the parameters in Table I [10,16]. We have removed spatial filtering by setting $k_0 = \infty$ because this only makes a slight difference to the results. The main features shown in Fig. 11 are that γ falls off with distance, with a faster decrease at higher frequencies. This is because the only term that depends on R in (75) is $\mathrm{Im}[K_0(q^*R)]$, but $|\mathrm{Im}(q^*)|$ is greater for higher frequencies and here the rate of decrease of $|\mathrm{Im}[K_0(q^*R)]|$ with R in Eq. (75) is more rapid. Coherence tends to fall slightly faster with R than in one dimension [16], owing to the greater predominance of high-k modes, as reflected in the asymptotic properties of the Macdonald function in Eq. (75) [16]. Indeed, the Macdonald function $K_0(q^*R) \to 0$ as $|q| \to \infty$. The coherence persists to large R at the spectral resonances, particularly the alpha and beta peaks near 9.3 and 18.5 Hz, respectively. These results are in accord with Eq. (75) and with prior results [16,28], where we showed that long-range coherence can only exist when q^2 is near the negative real axis (as seen for our spectral peaks in Fig. 3), where waves are weakly damped and can thus propagate over long distances. The figure demonstrates that when instability is approached, the coherence function tends to become spatially uniform at the instability frequency, potentially a useful diagnostic for detecting the approach to generalized seizure onset [6,21,28,29].

Figure 12 shows the 2D infinite planar geometry correlation functions obtained by inverse Fourier transforming Eq. (77) and using the parameters in Table I. These parameters correspond to an eyes-closed state. The figure demonstrates peaks at times that are approximately $2\pi/\xi$, where ξ is the dominant frequency. Furthermore, the correlation function goes to zero as $|T|$ and $|R|$ go to ∞.

B. Spherical brain geometry

The coherence function for the spherical geometry, in the limit $l_0 \to \infty$, is given by

$$\gamma(\theta,\omega) = \frac{g'(\theta,\omega)}{g'(0,\omega)}, \tag{81}$$

where

$$g'(\theta,\omega) = \frac{|A(\omega)|^2}{4\pi R_s^2}\sum_{\ell=0}^{\infty}\frac{2\ell+1}{\left|\ell(\ell+1)r_e^2/R_s^2 + q^2 r_e^2\right|^2}P_\ell(\cos\theta), \tag{82}$$

$$g'(0,\omega) = \frac{|A(\omega)|^2}{4\pi R_s^2}\sum_{\ell=0}^{\infty}\frac{2\ell+1}{\left|\ell(\ell+1)r_e^2/R_s^2 + q^2 r_e^2\right|^2}. \tag{83}$$

Due to the Wiener-Khintchine theorem, the correlation function $C(\theta,T) = \langle\phi_e(\theta,t+T)\phi_e(\theta,t)\rangle$ can be obtained by inverse Fourier transforming the cross spectrum $P(\theta,\omega)$ and is given by

$$C(\theta,T) = \frac{1}{2\pi}\int P(\theta,\omega)e^{-i\omega T}d\omega \tag{84}$$

$$= \frac{1}{8\pi^2 R_s^2}\int |A(\omega)|^2 e^{-i\omega T}\sum_{\ell=0}^{\infty}\frac{2\ell+1}{\left|\ell(\ell+1)r_e^2/R_s^2 + q^2 r_e^2\right|^2}P_\ell(\cos\theta)d\omega. \tag{85}$$

The normalized correlation function is

$$\rho(\theta,T) = \frac{g''(\theta,T)}{g''(0,0)}, \tag{86}$$

where

$$g''(\theta,T) = \frac{1}{8\pi^2 R_s^2}\int |A(\omega)|^2 e^{-i\omega T}\sum_{\ell=0}^{\infty}\frac{2\ell+1}{\left|\ell(\ell+1)r_e^2/R_s^2 + q^2 r_e^2\right|^2}P_\ell(\cos\theta)d\omega, \tag{87}$$

$$g''(0,0) = \frac{1}{8\pi^2 R_s^2}\int |A(\omega)|^2 \sum_{\ell=0}^{\infty}\frac{2\ell+1}{\left|\ell(\ell+1)r_e^2/R_s^2 + q^2 r_e^2\right|^2}d\omega. \tag{88}$$

Figure 13 shows the 2D spherical coherence function obtained from Eq. (81) for the parameters in Table I. At fixed frequency, the coherence function decays monotonically as θ increases, as in the planar geometry; the decrease is faster at higher frequencies. However, the decay in the coherence as the frequency increases, for fixed θ, is not monotonic, as in the planar geometry; the coherence persists to large θ at spectral resonances, particularly the alpha and beta peaks near 8.9 and 18.2 Hz, respectively, and near $f = 0$.

Figure 14 shows the normalized correlation function for the spherical geometry. The qualitative features are similar to those of the 2D planar geometry, with the correlation decreasing with both θ and T and there being a peak at a time lag approximately equal to $1/f_\alpha$, where f_α is the frequency of the alpha peak. A difference is that the correlation decreases more quickly as the distance increases in the spherical geometry compared to the planar geometry, where the distance in the spherical geometry is given by $R = R_s\theta$. Note that there is an even stronger peak at zero time lag, which reflects the fact that much of the activity is in the lowest mode, which is globally spatially uniform.

VI. SUMMARY AND DISCUSSION

In this work we have studied the spectral properties of an established corticothalamic neural field model in planar and spherical geometries to explore the effects of geometry on measures of brain activity. In the spherical case we decomposed the noise, activity, coherence, and correlations using spherical harmonics, motivated by a recent study that demonstrated that these closely approximate the eigenmodes of a folded cortical hemisphere [43]. This study yields equations for the modal dynamics, spectra, correlations, and coherence response functions. These equations incorporate both modal and corticothalamic resonances and explain how these phenomena depend on geometry and affect experimental observations. The following are our main results.

(i) Using the generalized NFT transfer function for the corticothalamic system, we have calculated the power spectrum for infinite planar, finite planar, and spherical geometries in Eqs. (39), (42), and (52). In the finite cases our results showed discrete modal effects on white-noise-driven spectra. We observed at the low-frequency part of the spectrum the uniform mode produces a spectral peak with f^{-2} behavior for spherical and finite geometries but f^{-1} in the infinite planar geometries.

(ii) We found that modal effects are strong near the corticothalamic resonances and can combine to produce substructure near the alpha peak if corticothalamic feedback is strong [6]. The modal effects also lead to a large enhancement in the low-frequency part of the spectrum.

(iii) We varied the radius R_s of the spherical brain and the linear size L_x of the finite planar case. We found that as $R_s \to \infty$ and $L_x \to \infty$ the spherical, finite, and infinite planar geometries approach one another, as expected on physical grounds.

(iv) We truncated the mode numbers in the expansion at $m_{\max}$ in the planar geometry. We found that the visible modal structure can be obtained with $m_{\max} = 3$ up to 30 Hz. The

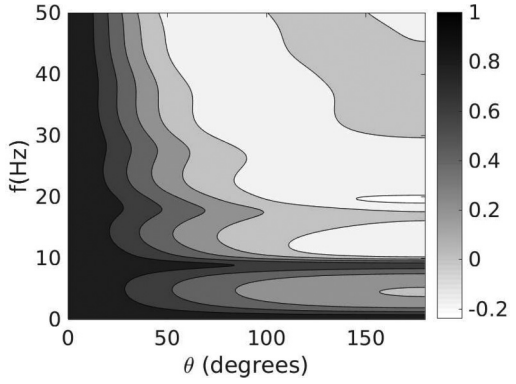

FIG. 13. Plot of the normalized coherence function $\gamma(\theta,\omega)$ vs θ and $f = \omega/2\pi$ for a spherical geometry, the parameters in Table I, and $R_s = 0.1$ m.

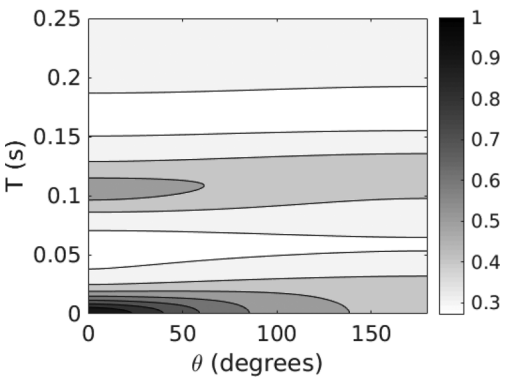

FIG. 14. Plot of the normalized correlation $\rho(\theta,T)$ vs θ and T of the spherical geometry, for the parameters in Table I with $R_s = 0.1$ m.

low-frequency enhancement for the $m = 0$ mode (i.e., the spatially uniform mode) has $P(f) \sim f^{-2}$. We also truncated the mode numbers in the expansion at $L_{\max}$ in the spherical geometry. We found that the number of modes required for an accurate representation of the power spectrum increases as the frequency increases. At $f = 0$ Hz, $L_{\max} \approx 1$ is required, whereas $L_{\max} \approx 5$–6 is required at $f \approx 100$ Hz.

(v) The cross spectrum has been calculated for the infinite planar and spherical geometries in Eqs. (59) and (69). There is no great qualitative change in either the power spectrum or the cross spectrum between geometries, except that the low-frequency spectrum in the infinite planar geometry is $1/f$, whereas in the spherical geometry it is $1/f^2$ because of the partitioning of energy into discrete modes. At small θ the low-frequency cross spectrum is stronger than in the infinite planar geometry and the alpha peak is sharper and stronger, again due to the partitioning of the energy into discrete modes.

(vi) The coherence has also been calculated for the infinite planar and spherical geometries in Eqs. (75) and (81). The normalized coherence function for the infinite planar geometry falls off with distance, with a faster decrease at higher frequencies due to the dependence on R in (75) and more slowly at resonances. Its rate of decrease as R increases is slightly faster than in one dimension due to the asymptotic properties of the Macdonald function in (75). For the spherical geometry, the normalized coherence function decays monotonically as θ increases at a fixed frequency in Eq. (81). As in the planar geometry, the coherence persists to large θ at spectral resonances, which are projected across the whole brain.

(vii) Correlation functions have also been calculated for the infinite planar and spherical geometries in Eqs. (77) and (86). For the planar geometry the normalized correlation function goes to zero as $|T|$ and $|R|$ go to ∞. In the spherical geometry, the features are similar to those of the 2D planar geometry, with the correlation decreasing with both θ and T. The correlation between two points decreases more quickly as their separation increases in the spherical geometry than in the planar geometry, where the separation in the spherical geometry is given by $R = R_s\theta$.

Overall, we find that modal effects in spherical and finite planar geometries are most important near resonances, particularly the low-frequency resonance at $f = 0$, where they lead to large enhancements in responses, correlations, and coherence. The present analysis for the spherical geometry will enable more realistic modeling and analysis of experimental brain signals in the future, particularly given the strong parallels between exact brain modes and spherical harmonics that have been established in recent works, as discussed in the Introduction.

ACKNOWLEDGMENTS

We thank N. Roy for helpful discussions on neural field theory and E. Muller for assistance with Fig. 1. We also thank Dr. Xiao (Demi) Gao for assistance with the figures. This work was supported by a University of Sydney International Scholarship, by the Australian Research Council Center of Excellence for Integrative Brain Function (Grant No. CE140100007), and by the Australian Research Council Laureate Fellowship Grant No. FL140100025.

[1] S. Coombes, Biol. Cybern. **93**, 91 (2005).
[2] G. Deco, V. K. Jirsa, P. A. Robinson, M. Breakspear, and K. Friston, PLoS Comput. Biol. **4**, e1000092 (2008).
[3] B. Ermentrout, Rep. Prog. Phys. **61**, 353 (1998).
[4] W. J. Freeman, *Mass Action in the Nervous System* (Academic, New York, 1975).
[5] M. A. Buice and J. D. Cowan, Phys. Rev. E **75**, 051919 (2007).
[6] P. A. Robinson, P. N. Loxley, S. C. O'Connor, and C. J. Rennie, Phys. Rev. E **63**, 041909 (2001).
[7] P. C. Bressloff and J. D. Cowan, Physica D **173**, 226 (2002).
[8] S. I. Amari, Biol. Cybern. **27**, 77 (1977).
[9] P. A. Robinson, C. J. Rennie, J. J. Wright, H. Bahramali, E. Gordon, and D. L. Rowe, Phys. Rev. E **63**, 021903 (2001).
[10] P. A. Robinson, C. J. Rennie, and D. L. Rowe, Phys. Rev. E **65**, 041924 (2002).
[11] P. A. Robinson, C. J. Rennie, and J. J. Wright, Phys. Rev. E **56**, 826 (1997).
[12] C. J. Rennie, P. A. Robinson, and J. J. Wright, Phys. Rev. E **59**, 3320 (1999).
[13] J. J. Jirsa and D. T. J. Liley, Behav. Brain Sci. **19**, 285 (1996).
[14] R. G. Abeysuriya, C. J. Rennie, P. A. Robinson, and J. W. Kim, Clin. Neurophysiol. **125**, 2016 (2014).
[15] S. C. O'Connor and P. A. Robinson, Phys. Rev. E **70**, 011911 (2004).
[16] P. A. Robinson, C. J. Rennie, D. L. Rowe, S. C. O'Connor, S. C. Gordon, and R. W. Whitehouse, Neuropsychopharmacology **28**, 74 (2003).
[17] S. J. van Albada, C. C. Kerr, A. K. I. Chiang, C. J. Rennie, and P. A. Robinson, Clin. Neurophysiol. **121**, 21 (2010).
[18] C. J. Rennie, P. A. Robinson, and J. J. Wright, Biol. Cybern. **86**, 457 (2002).
[19] R. G. Abeysuriya, C. J. Rennie, and P. A. Robinson, J. Neurosci. Methods **253**, 55 (2015).
[20] R. G. Abeysuriya and P. A. Robinson, J. Neurosci. Methods **258**, 28 (2016).
[21] K. K. Jerger, I. T. Netoff, T. J. Francis, T. Sauer, L. Pecora, L. S. Weinstein, and J. S. Schiff, J. Clin. Neurophysiol. **18**, 259 (2001).
[22] M. Breakspear, Hum. Brain Mapp. **15**, 175 (2002).
[23] M. Le Van Quyen, J. Martinerie, C. Adam, and F. J. Varela, Phys. Rev. E **56**, 3401 (1997).
[24] C. C. Kerr, C. J. Rennie, and P. A. Robinson, Biol. Cybern. **98**, 171 (2008).
[25] P. A. Robinson, R. W. Whitehouse, and C. J. Rennie, Phys. Rev. E **68**, 021922 (2003).
[26] S. C. O'Connor, P. A. Robinson, and A. K. I. Chiang, Phys. Rev. E **66**, 061905 (2002).
[27] S. C. O'Connor and P. A. Robinson, Phys. Rev. E **67**, 051912 (2003).

[28] P. L. Nunez, *Neocortical Dynamics and Human EEG Rhythms* (Oxford University Press, New York, 1995).
[29] E. Niedermeyer and F. H. Lopes da Silva, *Electroencephalography: Basic Principles, Clinical Applications, and Related Fields*, 4th ed. (Williams and Wilkins, Baltimore, 1999), Chaps. 9, 13, and 27.
[30] R. W. Thatcher, P. J. Krause, and M. Hrybyk, J. Clin. Neurophysiol. **64**, 123 (1986).
[31] P. A. Robinson, C. J. Rennie, D. L. Rowe, and S. C. O'Connor, Hum. Brain Mapp. **23**, 53 (2004).
[32] S. Visser, R. Nicks, O. Faugeras, and S. Coombes, Physica D **349**, 27 (2017).
[33] R. A. Yotter, R. Dahnke, P. M. Thompson, and C. Gaser, Hum. Brain Mapp. **32**, 1109 (2011).
[34] R. Srinivasan, P. L. Nunez, and R. B. Silberstein, IEEE Trans. Biomed. Eng. **45**, 814 (1998).
[35] P. L. Nunez, *Electric Fields of the Brain: The Neurophysics of EEG* (Oxford University Press, New York, 1981).
[36] L. Shen and M. K. Chung, *Proceedings of the Third International Symposium on 3D Data Processing, Visualization and Transmission* (Wiley, New York, 2006), p. 294.
[37] S. K. Law, P. L. Nunez, and R. S. Wijesinghe, IEEE Trans. Biomed. Eng. **40**, 145 (1993).
[38] P. L. Nunez, R. Srinivasan, A. F. Westdorp, R. S. Wijesinghe, D. M. Tucker, R. B. Silberstein, and P. J. Cadusch, Electroenceph. Clin. Neurophysiol. **103**, 499 (1997).
[39] P. L. Nunez, Math. Biosci. **21**, 279 (1974).
[40] P. L. Nunez, Brain Topogr. **1**, 199 (1989).
[41] P. L. Nunez, R. B. Silberstein, P. J. Cadusch, R. S. Wijesinghe, A. F. Westdorp, and R. Srinivasan, Electroenceph. Clin. Neurophysiol. **90**, 40 (1994).
[42] M. Breakspear and C. J. Stam, Philos. Trans. Biol. Sci. **360**, 1051 (2005).
[43] P. A. Robinson, X. Zhao, K. M. Aquino, J. D. Griffiths, S. Sarkar, and G. Mehta-Pandejee, NeuroImage **142**, 79 (2016).
[44] C. Brechbühler, G. Geirg, and O. Kübler, Comput. Vis. Image Understand. **61**, 154 (1995).
[45] G. Gerig, M. Styner, D. Jones, D. Weinberger, and J. Lieberman, in *Proceedings of the IEEE Workshop on Mathematical Methods in Biomedical Image Analysis, Hawaii, 2001* (Wiley, New York, 2001), p. 171.
[46] B. Gutman, Y. Wang, L. M. Lui, T. F. Chan, and P. M. Thompson, in *Proceedings of the 18th International Conference on Pattern Recognition*, *Hong Kong, 2006* (Wiley, New York, 2006), p. 964.
[47] A. Kelemen, G. Szekely, and G. Gerig, IEEE Trans. Med. Imaging **18**, 828 (1999).
[48] M. E. Shenton, G. Gerig, R. W. McCarley, G. Székely, and R. Kikinis, Psych. Res. NeuroImaging **115**, 15 (2002).
[49] P. M. Thompson and A. W. Toga, Trans. Med. Imaging **15**, 402 (1996).
[50] J. A. Roberts and P. A. Robinson, Phys. Rev. E **85**, 011910 (2012).
[51] S. J. van Albada, C. J. Rennie, and P. A. Robinson, J. Integr. Neurosci. **6**, 279 (2007).
[52] P. A. Robinson, C. J. Rennie, D. L. Rowe, S. C. O'Connor, and E. Gordon, Philos. Trans. R. Soc. B **360**, 1043 (2005).
[53] P. A. Robinson, C. J. Rennie, J. J. Wright, and P. D. Bourke, Phys. Rev. E **58**, 3557 (1998).
[54] J. J. Wright and D. T. J. Liley, Network **5**, 191 (1994).
[55] D. L. Rowe, P. A. Robinson, C. J. Rennie, A. W. Harris, K. L. Felmingham, I. L. Lazzaro, and E. Gordon, J. Integr. Neurosci. **3**, 453 (2004).
[56] P. L. Nunez and R. Srinivasan, *Electric Fields of the Brain: The Neurophysics of EEG* (Oxford University Press, New York, 2006).
[57] V. K. Jirsa, K. J. Jantzen, A. Fuchs, and J. A. Kelso, IEEE Trans. Med. Imag. **21**, 493 (2002).
[58] F. W. J. Olver, D. W. Lozier, R. F. Boisvert, and C. W. Clark, *NIST Handbook of Mathematical Functions* (Cambridge University Press, Cambridge, 2010).
[59] P. A. Robinson, Phys. Rev. E **72**, 011904 (2005).
[60] P. A. Robinson, J. R. Soc. Interface **14**, 20160994 (2017).
[61] G. Arfken, *Mathematical Methods for Physicists*, 3rd ed. (Academic, Orlando, 1985), Chap. 12.8.
[62] E. R. Kandel, J. H. Schwartz, and T. M. Jessell, *Principles of Neural Science*, 4th ed. (McGraw-Hill, New York, 2000), Chap. 22.
[63] A. V. Oppenheim and R. W. Schafer, *Discrete-Time Signal Processing* (Prentice-Hall, Englewood Cliffs, 1989).
[64] J. C. Shaw, J. Med. Eng. Technol. **5**, 279 (1981).